Quasiperiodic fluctuations of von Kármán turbulence driven by viscous stirring

Ryo Araki ●[1,2,*] and Susumu Goto ●[1]

[1]*Graduate School of Engineering Science, Osaka University, 1-3 Machikaneyama,*
Toyonaka, Osaka 560-8531, Japan
[2]*Université Lyon, École Centrale de Lyon, CNRS, Université Claude Bernard Lyon 1,*
INSA Lyon, LMFA, UMR5509, 69130 Écully, France

We numerically simulate the von Kármán swirling flow driven by viscous stirring with a pair of inversely rotating smooth disks at moderate Reynolds numbers well beyond the first Hopf bifurcation. Despite the time-independent driving mechanism, quantities such as the kinetic energy and its dissipation rate fluctuate quasiperiodically with a period longer than the disk rotation period. We employ the toroidal-poloidal and boundary-bulk decompositions to explain the quasiperiodic fluctuations, which are always observed in the examined Reynolds-number range, and a nontrivial relation between the energy input and dissipation rates. The toroidal-poloidal decomposition of the energy reveals that the quasiperiodic fluctuations originate from the exchange of the two energy components; the growth of the toroidal energy E^{tor} leads to the growth of the poloidal energy E^{pol} due to the centrifugal instability, whereas the growth of E^{pol} leads to the decay of E^{tor} due to the angular momentum transfer. The boundary-bulk decomposition distinguishes the qualitatively different dynamics coexisting in the system, which explains the nontrivial energy cycle.

I. INTRODUCTION

The kinetic energy E and its dissipation rate ϵ of statistically steady turbulence driven by steady force can significantly oscillate in time and sometimes reveal a quasiperiodic behavior. For example, the mean kinetic energy of turbulence sustained by a steady body force in a periodic cube quasiperiodically oscillates in time with a period of $\mathcal{O}(10T_e)$, where T_e denotes the largest-scale eddy turnover time, with a magnitude of about 10% of its mean [1,2]. This quasiperiodic behavior is associated with energy cascading events. More precisely, it takes a finite time for the energy to cascade down to smaller scales, and it also takes a finite time for the energy to be restored by the external force. The period of the system oscillation is determined by these two timescales [2]. These timescales are almost independent of the Reynolds number Re, and the quasiperiodicity of developed turbulence might be related to periodic behavior, at low Reynolds numbers. Since the quasiperiodicity leads to unbalance between the energy flux and dissipation [3], namely, the nonequilibrium nature of turbulence [4], it is important to investigate whether the periodic behavior can occur in more realistic systems. In the present study, we demonstrate a similar type of quasiperiodic behavior of turbulence driven by realistic forcing in a container and unveil the physical mechanism of the observed energy cycle.

---

*r_araki@fm.me.es.osaka-u.ac.jp
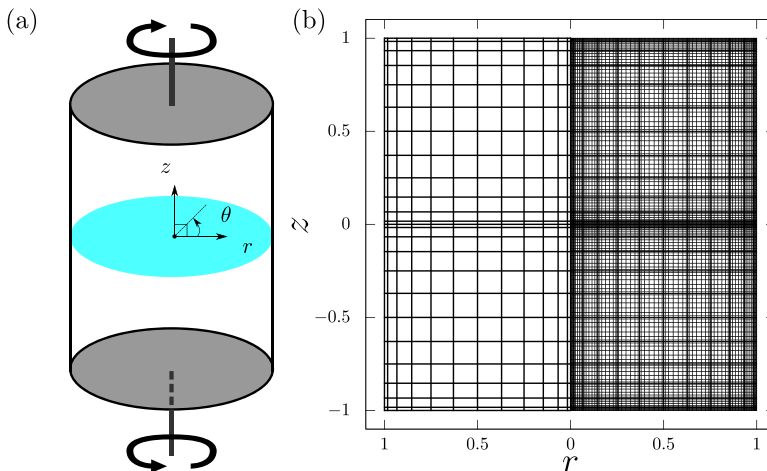
FIG. 1. (a) Schematic of von Kármán flow with viscous stirring. (b) Discretization on the meridional plane corresponding to the low-resolution setup; elements and their seventh-order discrete weight points are shown in the left and right planes, respectively.

For this purpose, we numerically investigate the flow between a pair of counter-rotating disks in a cylindrical container, namely, the von Kármán swirling flow [Fig. 1(a)]. The characteristics of this flow are different depending on whether the disks are smooth (viscous stirring) or rough (inertial stirring) [5]. For example, the nondimensionalized energy dissipation rate $C_\epsilon = \epsilon/(u'^3/L)$, where u' and L are characteristic velocity and length scale, is independent of the Reynolds number Re for inertial stirring, whereas C_ϵ depends on Re for viscous stirring, although C_ϵ is independent of Re if we consider the dissipation only in the bulk.

Since we can conduct experiments at relatively high Re with bladed disks (i.e., inertial stirring), many authors experimentally investigated this system to discuss the statistics of high-Re turbulence such as fluid acceleration [6], possible singularities of the solution of the Navier-Stokes equation [7], intermittency [8,9], and interscale energy transfer [10]. Furthermore, the von Kármán flow with inertial stirring sometimes shows interesting behaviors such as bistable turbulent states [11] and related slow reversal of the flow [12].

Remarkably, the energy input rate P by the bladed disks oscillates significantly in time with an amplitude of about 10% of its mean [13,14]. Labbé *et al.* [13] conducted experiments with air to show that P significantly oscillated in time, and Pinton *et al.* [14] showed that the probability density function of P is independent of Re and its non-Gaussianity is due to the large-scale coherent structure. They also showed that the decay of a strong P event takes a long time of about 20 times the period of the disk rotation. Titon *et al.* [15] conducted water experiments to compare the constant-rotation and constant-torque cases. They showed that the former led to larger oscillations of P and that there was a time delay between P and the pressure fluctuations. Aumaitre *et al.* [16] investigated the long-distance correlation by using sensors embedded in the blades. Furthermore, Marié *et al.* [17] showed the importance of large-scale structures for the angular velocity transport and indicated its importance in the energy transport, and Kuzzay *et al.* [18] discussed the energy cycle by using the generalized Kármán-Howarth equation.

Although numerical simulations are more suitable for the investigation of the origin of these large fluctuations of the von Kármán turbulence, compared to experimental studies, a much smaller number of numerical studies were conducted, and many of them were motivated by the investigation of dynamo [19–21]. Poncet *et al.* [22] numerically demonstrated the mean flow structures at high Reynolds numbers by using a Reynolds stress model, for both viscous and inertial stirrings. Kreuzahler *et al.* [23] used a numerical code for periodic turbulence and the penalization method

to conduct direct numerical simulations (DNS) of von Kármán turbulence with inertial stirring, and they showed that large-scale structures are similar to those observed in experiments at higher Reynolds numbers. Furthermore, Nore and her co-workers also conducted DNS [20] and large-eddy simulations [21] for the dynamo in von Kármán turbulence with bladed disks. For smooth disks (viscous stirring), Nore [24] numerically investigated the linear stability. Shen *et al.* [25] examined numerically, by the finite element method, the instability to compare the critical curves theoretically predicted in Ref. [26].

In the present study, we conduct DNS by a spectral element method (SEM) of viscous stirred von Kármán turbulence. Note that, in the present study, we use the word *turbulence* to express complex flow observed at moderate Reynolds numbers ($1000 \leqslant \mathrm{Re} \leqslant 3000$), which are well beyond the critical Reynolds number for the first Hopf bifurcation, but smaller than the Reynolds number [say, $\mathrm{Re} = \mathcal{O}(10^4)$ [27]] for fully developed turbulence to be sustained.

We show that despite the steady stirring (note that the boundary condition is time independent), the quantities such as kinetic energy and its dissipation rate temporally oscillate in a quasiperiodic manner. The period of the oscillation is about a six rotation period of the disks. By decomposing the kinetic energy into the toroidal and poloidal components, we can describe the physical origin of the quasiperiodic energy cycle. Furthermore, the boundary-bulk decomposition explains the coexistence of the well-balanced dynamics in the vicinity of the rotating disks and the time-delayed dynamics in the bulk of the flow. In the following sections, we explain a nontrivial phase difference between the energy input and dissipation rates by combining the energy cycle with the coexisting two different dynamics, and further discuss the robustness of the quasiperiodicity.

II. NUMERICAL SETUP

We conduct DNS of the von Kármán swirling flow [Fig. 1(a)] in a cylindrical vessel with radius R and height H. Here, we set $H = 2R$, so that the aspect ratio $H/R = 2$. A pair of smooth disks are counter-rotating with a common constant period T. We define the cylindrical coordinates (r, θ, z) as shown in Fig. 1(a). We impose nonslip boundary conditions for the nondimensional velocity field u on the vessel wall and the rotating disks. In the present study, we normalize the length and time-scales by R and $T/2\pi$, respectively. Then, the Reynolds number is defined by

$$\mathrm{Re} = \frac{2\pi R^2}{\nu T}, \tag{1}$$

where ν is the kinematic viscosity of the fluid.

We numerically solve the Navier-Stokes equation,

$$\frac{\partial u_i}{\partial t} + u_j \frac{\partial u_i}{\partial x_j} = -\frac{\partial p}{\partial x_i} + \frac{1}{\mathrm{Re}} \frac{\partial u_i}{\partial x_j \partial x_j}, \tag{2}$$

and the continuity equation,

$$\frac{\partial u_i}{\partial x_i} = 0, \tag{3}$$

for an incompressible fluid with a constant density, which we set to unity. Here, p denotes the nondimensional pressure field.

We have developed a spectral-element-Fourier-method code [28], which combines the one-dimensional Fourier spectral method in the azimuthal direction and a two-dimensional SEM in the meridional plane. The SEM uses high-order base functions (in the present DNS, we use the seventh order boundary-interior decomposed Gauss-Lobatto-Legendre polynomials) in each element to achieve both spectral accuracy and spatial flexibility. We employ two sets of resolutions, namely the low-resolution setup for long computations at moderate Reynolds numbers and the high-resolution setup to investigate a higher Re case. In the low-resolution setup, we use 256 Fourier modes for the azimuthal direction with (24, 12) elements in the (z, r) directions, as shown in Fig. 1(b). Elements

are densely arranged for regions with strong velocity gradients near the rotating disks and the sidewall. We use 512 Fourier modes and $(48, 24)$ elements on (z, r) planes for the high-resolution setup. We have also implemented an adaptive parallelization algorithm [29] over both Fourier modes and spectral elements to conduct highly parallelized simulations. Details of the algorithm can be found in the textbook [30].

As we mentioned in the Introduction, the objective of the present study is to reveal the origin of the quasiperiodic energy cycle. We may expect that this feature is observed irrespective of Re beyond the critical value for the instability of the steady flow. Stability analysis in the flow driven by smooth disks was conducted in Ref. [24] to show that the critical Re for the Hopf bifurcation is about 350, and we conduct DNS of turbulence at three different values of the Reynolds number: Re = 1000, 1500, and 3000. We begin our DNS with the low-resolution setup. We initialize the velocity field with swirling flow consistent with the boundary conditions on which we impose small disturbances, then gradually increase Re to obtain a statistically steady turbulent state at Re = 1000 and 1500. Then, we interpolate the velocity field to the high-resolution grid to further increase Re up to 3000. The flow exhibits quasiperiodic fluctuations for all three values of Re, and we will focus on the intermediate value of Re(= 1500), where we obtain a $200T$ long dataset of flow fields saved every $0.08T$. We will show the Reynolds-number dependence of the flow in Sec. III D.

III. RESULTS

A. Quasiperiodic cycle of energy

First, we show the quasiperiodic temporal evolution of the energy,

$$E = \int \frac{1}{2} u_i u_i d\Omega, \tag{4}$$

its input rate,

$$P_{\text{vis}} = \frac{1}{\text{Re}} \int \frac{\partial}{\partial x_j} \left(\frac{\partial u_i}{\partial x_j} u_i \right) d\Omega, \tag{5}$$

and its dissipation rate,

$$\epsilon = \frac{1}{\text{Re}} \int \frac{\partial u_i}{\partial x_j} \frac{\partial u_i}{\partial x_j} d\Omega. \tag{6}$$

Here, Ω denotes the system domain. We may derive the energy equation,

$$\frac{dE}{dt} = P_{\text{vis}} - \epsilon, \tag{7}$$

in the present system by multiplying (2) by u_i and spatial integration.

We plot the time series of E, P_{vis}, and ϵ in Fig. 2(a) to observe time variations despite the time-independent boundary conditions. It is further important to observe in Fig. 2(a) that the time fluctuations are quasiperiodic. Note that the figure shows the values normalized by their temporal average and standard deviation (see Table I) to focus on their phase difference. Although the temporal fluctuations of these quantities are not large (e.g., the standard deviation of E is about 1% of $\overline{E}$), we will show, in the next subsection, that there exists a significant energy cycle in the system; note that some quantities in Table I such as E^{pol} or $\mathcal{T}^{\text{tp}}$, which we define in Sec. III B, have large standard deviations.

Figure 2(b) shows the time series of the energy input rate P_{vis} and the dissipation rate ϵ. The system evolves quasiperiodically with a period of about $6T$. However, this graph shows clockwise rotations. This means that the increase of P_{vis} is followed by a decrease, rather than an increase, of ϵ. Therefore, we cannot describe these dynamics by the standard energy cascade picture, in which the energy dissipation rate follows the input rate. The goal of the present paper is to describe the energy
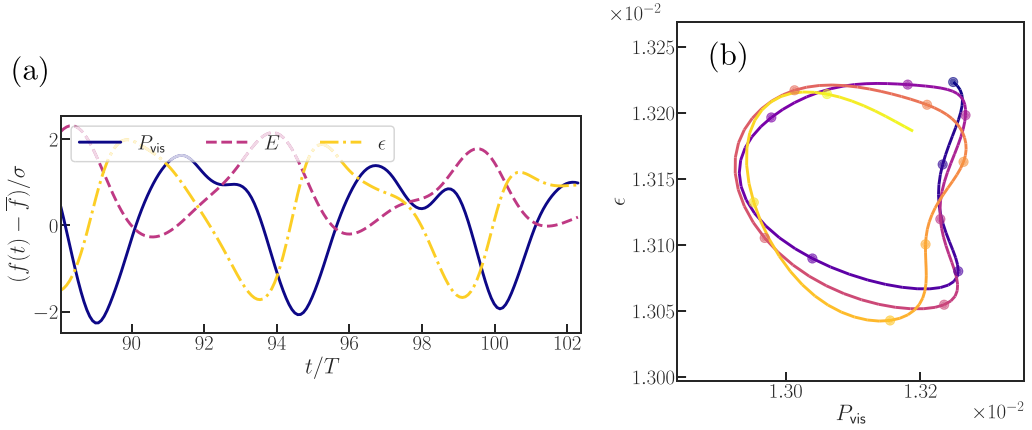
FIG. 2. (a) Time series of the energy input rate P_{vis}, the energy E, and the energy dissipation rate ϵ. We show the values normalized by their time average $\overline{f}$ and standard deviation σ estimated over $200T$. The time average and standard deviation of each quantity are shown in Table I. (b) two-dimensional (2D) diagram of P_{vis} and ϵ. The dark to light color gradient represents the temporal evolution. The time increment between two successive dots is T. Results for Re $= 1500$.

cycle of smooth disk stirred (i.e., viscous stirred) von Kármán flow and understand the physics behind the quasiperiodic temporal evolution shown in Fig. 2.

B. Toroidal-poloidal decomposition of the energy

A key to the understanding of the quasiperiodic behavior is the toroidal-poloidal decomposition of the energy. More concretely, we decompose the total energy E into E^{tor} associated with the toroidal velocity component and E^{pol} with the poloidal component:

$$E^{\text{tor}} = \int \frac{1}{2} u_\theta^2 d\Omega, \quad E^{\text{pol}} = \int \frac{1}{2}\left(u_z^2 + u_r^2\right) d\Omega. \tag{8}$$

We can derive the governing equations for these quantities from (7), which read

$$\frac{dE^{\text{tor}}}{dt} = P_{\text{vis}} - \epsilon^{\text{tor}} - \mathcal{T}^{\text{tp}} \quad \text{and} \quad \frac{dE^{\text{pol}}}{dt} = \mathcal{T}^{\text{tp}} - \epsilon^{\text{pol}}. \tag{9}$$

TABLE I. Time average $\overline{f}$ and standard deviation σ, normalized by the average, of each quantity. Results for Re $= 1500$.

f	$\overline{f}$	$\sigma/\overline{f}$ (%)	Figure	f	$\overline{f}$	$\sigma/\overline{f}$ (%)	Figure
E	1.06×10^{-2}	1.19	2	ϵ	1.31×10^{-2}	0.367	2
E^{tor}	8.82×10^{-3}	1.29	3, 5	ϵ^{tor}	1.14×10^{-2}	0.383	
E^{pol}	1.82×10^{-3}	8.03	3, 8	ϵ^{pol}	1.69×10^{-3}	1.09	3
$E^{\text{tor}}_{\text{bou}}$	5.11×10^{-3}	0.274	5	ϵ_{bou}	1.20×10^{-2}	0.490	5, 10
$E^{\text{tor}}_{\text{bulk}}$	3.71×10^{-3}	2.99	5	ϵ_{bulk}	1.10×10^{-3}	1.80	5, 11
$E^{\text{pol}}_{\text{bou}}$	2.83×10^{-4}	4.41	8	$\epsilon^{\text{pol}}_{\text{bou}}$	1.38×10^{-3}	0.912	
$E^{\text{pol}}_{\text{bulk}}$	1.53×10^{-3}	9.50	8	$\epsilon^{\text{pol}}_{\text{bulk}}$	3.05×10^{-4}	5.34	8
$\mathcal{T}^{\text{tp}}$	1.69×10^{-3}	8.36	3	$\mathcal{T}_{\text{bb}}$	1.10×10^{-3}	7.84	11
P_{vis}	1.31×10^{-2}	0.671	2, 3, 10, 11				
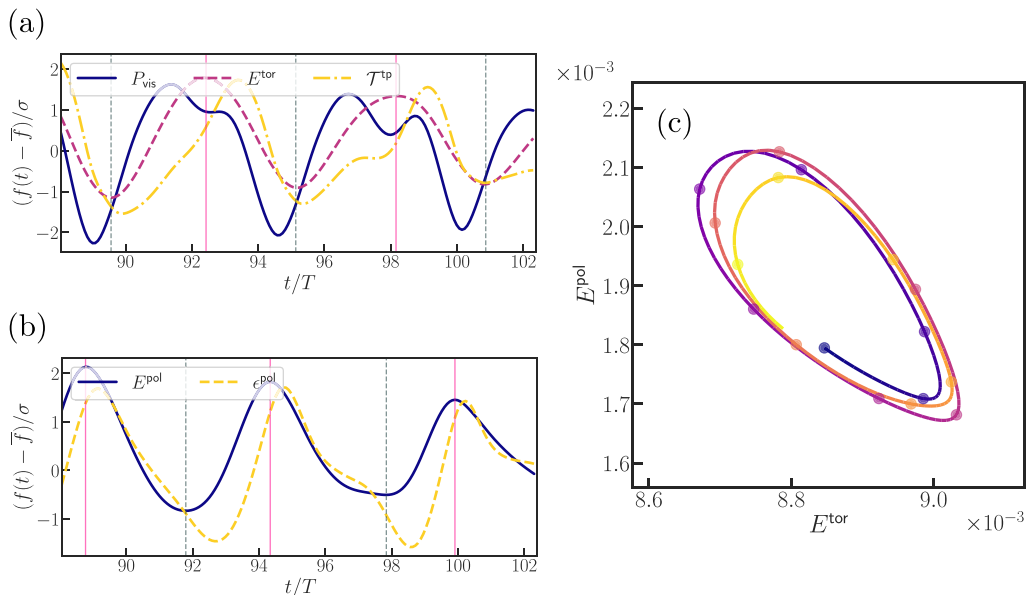
FIG. 3. (a) Time series of P_{vis}, E^{tor}, and $\mathcal{T}^{\mathrm{tp}}$. Pink and grey vertical lines indicate the local maxima and minima of E^{tor}, respectively. (b) Time series of E^{pol} and ϵ^{pol}. Pink and grey vertical lines indicate the local maxima and minima of E^{pol}, respectively. (c) 2D diagram of E^{tor} and E^{pol}. The time average and standard deviation of each quantity are shown in Table I. Results for Re = 1500.

In (9), ϵ^{tor} and ϵ^{pol} denote the associated energy dissipation rates,

$$\epsilon^{\mathrm{tor}} = \frac{1}{\mathrm{Re}} \int \nabla u_\theta \cdot \nabla u_\theta \, d\Omega \text{ and } \epsilon^{\mathrm{pol}} = \frac{1}{\mathrm{Re}} \int \nabla u_z \cdot \nabla u_z + \nabla u_r \cdot \nabla u_r d\Omega, \qquad (10)$$

and $\mathcal{T}^{\mathrm{tp}}$ represents the energy transfer from E^{tor} to E^{pol}, which plays an important role in the quasiperiodic fluctuations. We estimate $\mathcal{T}^{\mathrm{tp}}$ by computing the time derivative of E^{tor} and E^{pol}. We have confirmed that the thus estimated $\mathcal{T}^{\mathrm{tp}}$ is consistent with (9).

In the following, we describe the dynamics of the system in terms of E^{tor} and E^{pol}. First, we examine the temporal evolutions of E^{tor}, E^{pol}, P_{vis}, $\mathcal{T}^{\mathrm{tp}}$, and ϵ^{pol} in Fig. 3. Let us start with the time $t/T = 89.6$, when E^{tor} takes a local minimum [Fig. 3(a)]. At this stage, the flow is calm with a small toroidal swirling component. This means that there exists strong shear flow near the rotating disks, and then P_{vis} starts growing. In consequence, as observed in Fig. 3(a), P_{vis} accumulates energy in E^{tor} with a finite-time delay because it takes time to transmit the energy from the disks to the flow.

Next, we observe in Fig. 3(a) that the evolution of $\mathcal{T}^{\mathrm{tp}}$ follows that of E^{tor}. We can understand that the centrifugal instability of the developed swirling flow leads to this energy transfer. The growth of the instability takes time and it explains the time delays in the evolution of E^{tor} and $\mathcal{T}^{\mathrm{tp}}$.

By comparing Figs. 3(a) and 3(b), we see that the increase of E^{pol} follows that of $\mathcal{T}^{\mathrm{tp}}$. Again, the finite time delays between these quantities are due to the energy accumulation process in the poloidal component.

Figure 3(b) shows the time series of the energy dissipation rate ϵ^{pol} along with E^{pol}. These two quantities attain their local maxima at almost the same times with a small discrepancy (see, e.g., $t/T = 94.3$). This implies that the poloidal energy dissipation occurs by developed structures characterized by E^{pol}. The reason of this small time discrepancy and structures relevant to E^{pol} are further discussed in Appendix A. The increase of E^{pol} also triggers the depletion of E^{tor} as $\mathcal{T}^{\mathrm{tp}}$ transfers the energy from E^{tor} to E^{pol}. This leads to another local minimum of E^{tor} at $t/T = 95.1$. Then, the cycle returns to the beginning. It is worth emphasizing that the energy transfer from E^{tor}

TABLE II. Step-by-step description of the quasiperiodic energy cycle.

1.	$P_{\mathrm{vis}} \nearrow$	(local maximum at $t/T = 91.5$)	due to shear flow on the disks
2.	$E^{\mathrm{tor}} \nearrow$	(local maximum at $t/T = 92.3$)	due to P_{vis}
3.	$\mathcal{T}^{\mathrm{tp}} \nearrow$	(local maximum at $t/T = 93.0$)	due to the centrifugal instability
4.	$E^{\mathrm{pol}} \nearrow$	(local maximum at $t/T = 94.0$)	due to $\mathcal{T}^{tp}$
5.{	$\epsilon^{\mathrm{pol}} \nearrow$	(local maximum at $t/T = 94.4$)	due to E^{pol}
	$E^{\mathrm{tor}} \searrow$	(local minimum at $t/T = 95.1$)	due to the angular momentum transfer

to E^{pol} is accompanied by the transfer of the angular momentum. More precisely, as E^{pol} grows, the fast circulation near the disks and slow swirling in the bulk of the container are mixed, and E^{tor} is reduced.

Thus, the quasiperiodic fluctuations of the system with a period of about $6T$ can be explained by the toroidal-poloidal decomposition of the energy and the energy transfer $\mathcal{T}^{\mathrm{tp}}$ between E^{tor} and E^{pol}. As a consequence, their 2D plot shows an anticlockwise cycle [Fig. 3(c)]. We summarize the observed step-by-step energy cycle in Table II. Here, we emphasize again that the energy exchange between the toroidal and poloidal energy components plays an essential role in the quasiperiodic energy cycle. In fact, the temporal fluctuations of $\mathcal{T}^{\mathrm{tp}}$, and therefore E^{pol}, have significant magnitudes (Table I).

However, the nontrivial phase relation between P_{vis} and ϵ shown in Fig. 2(b) remains unsolved. To understand the relation, we need to evaluate how ϵ behaves in the different domains of the flow. We employ the boundary-bulk decomposition in the next subsection to deepen the analysis.

C. Boundary-bulk decomposition

The system has a strong toroidal velocity in the vicinity of the rotating disks. This boundary region is governed by viscous stress and shows different behavior compared to the rest (i.e., bulk) of the system. It is key to the following analysis to decompose the system into the boundary and bulk regions. This decomposition is related to the conclusion of Ref. [5]. For this purpose, we evaluate the normalized second invariant,

$$\widehat{Q} = \frac{\omega^2 - s^2}{\omega^2}, \tag{11}$$

of the velocity gradient tensor $V_{ij} = \partial u_i / \partial x_j$. Here, $s^2 = S_{ij} S_{ij}$ and $\omega^2 = \Psi_{ij} \Psi_{ij}$ with $S_{ij} = (V_{ij} + V_{ji})/2$ and $\Psi_{ij} = (V_{ij} - V_{ji})/2$. This quantity $\widehat{Q}$ evaluates the relative dominance of the enstrophy. We plot the average $\langle \widehat{Q} \rangle$ of $\widehat{Q}$ over time and the azimuthal direction in Fig. 4(a). This shows that, as expected, the enstrophy and squared strain rate tend to be balanced in the vicinity of rotating disks. By using $\langle \widehat{Q} \rangle$, we define the boundary region by

$$\Omega_{\mathrm{bou}} = \{ x | \langle \widehat{Q}(x) \rangle < \delta_{\mathrm{bou}} \text{ and } |z| \geqslant 0.9R \}, \tag{12}$$

where $\delta_{\mathrm{bou}} (> 0)$ is a threshold which we set to 0.2. We define Ω_{bulk} as the complement of Ω_{bou}. These two regions are visualized in Fig. 4(b).

Figures 5(a) and 5(b) show the results of boundary-bulk decomposition of E^{tor} and ϵ, respectively. Note that the quantities in these figures are not normalized by their standard deviations. The temporal fluctuations of E^{tor} are determined by its bulk component. This is explained by the fact that the energy injection is well balanced with the sum of the dissipation and transfer in the boundary region [Fig. 10(b) in Appendix B], and the energy in the boundary region hardly fluctuates. This is an interesting nontrivial result. Note that $E_{\mathrm{bou}}^{\mathrm{tor}}$ and $E_{\mathrm{bulk}}^{\mathrm{tor}}$ equally contribute to E^{tor}, but the fluctuations of E^{tor} are determined only by $E_{\mathrm{bulk}}^{\mathrm{tor}}$.

On the other hand, the temporal fluctuations of ϵ are determined by the boundary contribution [Fig. 5(b)] as the velocity gradient is much larger in the vicinity of the rotating disks. In fact, Fig. 5(c)
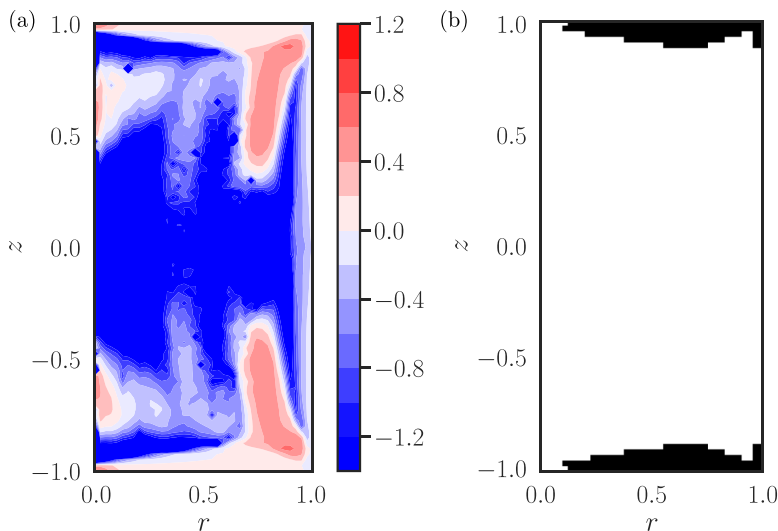
FIG. 4. (a) Average $\langle \widehat{Q} \rangle$ of the normalized second invariant of the velocity gradient tensor. (b) The boundary region defined by (12) is shaded. Results for Re = 1500.

shows that ϵ_{bou} synchronizes in antiphase with $E_{\text{bou}}^{\text{tor}}$. This antiphase synchronization is explained by the fact that the large value of $E_{\text{bou}}^{\text{tor}}$ corresponds to the small velocity gradient in the boundary, that is, the small value of ϵ_{bou} and vice versa. Note that the magnitude of ϵ is also determined by ϵ_{bou} (i.e., $\epsilon_{\text{bou}} \gg \epsilon_{\text{bulk}}$). Therefore, to understand the fluctuations of ϵ, we have to understand these of $E_{\text{bou}}^{\text{tor}}$. Although we do not have a clear description of the fluctuations of $E_{\text{bou}}^{\text{tor}}$ so far, it is reasonable
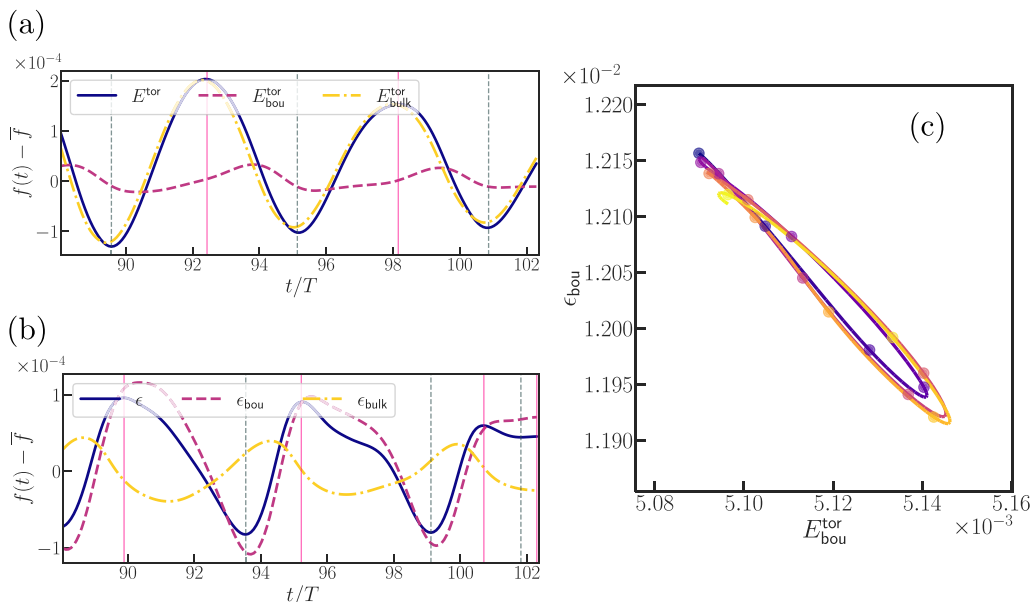
FIG. 5. (a) Time series of toroidal energy E^{tor} and its boundary-bulk decomposition. (b) Time series of energy dissipation ϵ and its boundary-bulk decomposition. (c) 2D diagram of $E_{\text{bou}}^{\text{tor}}$ and ϵ_{bou}. The time average and standard deviation of each quantity are shown in Table I. Results for Re = 1500.
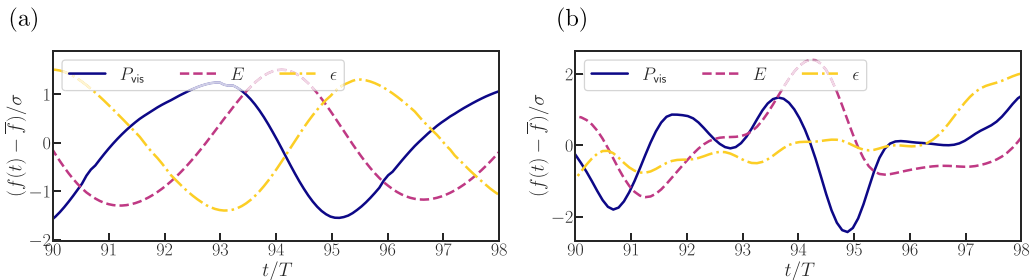
FIG. 6. Time series of the energy input rate P_{vis}, energy E, and energy dissipation rate ϵ at (a) Re $= 1000$ and (b) 3000. The values are normalized by their time average $\overline{f}$ and standard deviation σ. For Re $= 1000$, $\overline{P}_{\mathrm{vis}} = 7.67 \times 10^{-3}$ and σ is 0.43% of $\overline{P}_{\mathrm{vis}}$; $\overline{E} = 9.85 \times 10^{-3}$ and σ is 0.36% of $\overline{E}$; $\overline{\epsilon} = 7.67 \times 10^{-3}$ and σ is 0.12% of $\overline{\epsilon}$. For Re $= 3000$, $\overline{P}_{\mathrm{vis}} = 8.98 \times 10^{-3}$ and σ is 1.26% of $\overline{P}_{\mathrm{vis}}$; $\overline{E} = 8.51 \times 10^{-3}$ and σ is 0.75% of $\overline{E}$; $\overline{\epsilon} = 8.97 \times 10^{-3}$ and σ is 0.22% of $\overline{\epsilon}$.

that there is a phase difference between $E_{\mathrm{bulk}}^{\mathrm{tor}}$ and $E_{\mathrm{bou}}^{\mathrm{tor}}$ because it takes a finite time for the viscous stirring to drive toroidal flow in the bulk. Further analysis of the boundary-bulk decomposition is given in Appendix B.

These findings explain the nontrivial phase of P_{vis} against ϵ. The phase of ϵ is determined by its boundary component ϵ_{bou} [Fig. 5(b)], and it antisynchronizes with the boundary contribution $E_{\mathrm{bou}}^{\mathrm{tor}}$ of E^{tor} [Fig. 5(c)]. On the other hand, the phase of E^{tor} is almost identical to its bulk component $E_{\mathrm{bulk}}^{\mathrm{tor}}$ [Fig. 5(a)] and it has a time-delayed correlation with P_{vis} [Fig. 3(a)]. Therefore, the phase of P_{vis} does not have direct connection to that of ϵ and their 2D plot shows the nontrivial clockwise cycle [Fig. 2(b)].

D. Reynolds-number dependence

We have investigated, in detail, the case with the intermediate Reynolds number (Re $= 1500$) in the preceding subsections, and we have concluded that the quasiperiodic behavior of the system stems from the E^{tor}-E^{pol} cycle shown in Fig. 3(b). Here, we compare the results of Re $= 1000$, 1500, and 3000 to demonstrate that E^{tor}-E^{pol} cycles are observed irrespective of Re in the examined range.

Figure 6 shows the time series of P_{vis}, E, and ϵ in two different Reynolds numbers; see Fig. 2(a) for the Re $= 1500$ case. The quasiperiodicity is present in these lower and higher Re cases. The flow exhibits periodic cycles at Re $= 1000$ [Fig. 6(a)], while there are more complex dynamics at Re $= 3000$ [Fig. 6(b)]. In fact, although P_{vis}-ϵ plot at Re $= 3000$ does not show a clear clockwise cycle as in Fig. 2(b) (not shown), this is reasonable because the clockwise cycle is a result of nontrivial phase difference discussed in Sec. III C and is not a universal feature of the flow.

In Fig. 7, we show the 2D plots of $E^{\mathrm{tor}} - \overline{E^{\mathrm{tor}}}$ and $E^{\mathrm{pol}} - \overline{E^{\mathrm{pol}}}$ for the three different Reynolds numbers. The anticlockwise cycle of E^{tor}-E^{pol} is evident irrespective of Re. More concretely, we observe a periodic cycle at Re $= 1000$ with a smaller amplitude than the Re $= 1500$ case, and in the higher Reynolds number (Re $= 3000$) case, we still observe a quasi-periodic cycle. It is also an important observation that the period of the E^{tor}-E^{pol} cycle is always about 6 rotation period of the disks in the examined range of Re. By recalling that the Hopf bifurcation occurs at Re ≈ 350 [24], we can conclude that the quasi-cyclic behavior of E^{tor} and E^{pol} is a character which exists in a wide range of Re beyond the first bifurcation.

Note that time series at Re $= 3000$ show complex trajectories for longer computations, and we plot only one characteristic period in Fig. 7. We speculate that this quasiperiodicity persists behind the chaotic fluctuations in higher Reynolds numbers because we have observed a similar phenomenon in the periodic box turbulence [2]; a quasiperiodic behavior originates in periodic flow at low Re, and it survives, in a statistical sense, even in fully developed turbulence at much higher
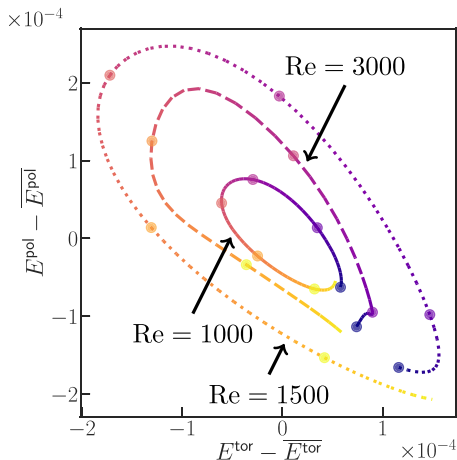
FIG. 7. 2D diagram of E^{tor} and E^{pol} for Re = 1000 (solid line), 1500 (dotted line), and 3000 (dashed line). We choose a characteristic cycle from time series and subtract the time average for visibility; $(\overline{E^{\text{tor}}}, \overline{E^{\text{pol}}}) = (7.96 \times 10^{-3}, 1.89 \times 10^{-3})$, $(8.82 \times 10^{-3}, 1.82 \times 10^{-3})$, and $(7.13 \times 10^{-3}, 1.40 \times 10^{-3})$ for Re = 1000, 1500, and 3000, respectively.

Re. However, statistical analysis with longer time series at Re = 3000 or even higher Re is beyond the capability of current numerical resources.

Here, we further discuss the Reynolds-number dependence of the proposed picture. For higher Reynolds numbers, (A) the turbulent boundary layer loses the well-synchronized relation of the energy injection and the sum of the dissipation and transfer [Fig. 10(b) in Appendix B] leading to a time delay between P_{vis} and $\epsilon_{\text{bou}} + \mathcal{T}_{\text{bb}}$, and (B) developed turbulence in the bulk generates a multiscale energy cascade, and nondirect energy dissipation occurs. It leads to time delayed peaks of $E_{\text{bulk}}^{\text{pol}}$ and $\epsilon_{\text{bulk}}^{\text{pol}}$, rather than synchronized ones [shown in Fig. 8(b) in Appendix A]. However, these time scales of the delayed dynamics are much shorter than that of the large-scale temporal fluctuations due to energy exchanges between E^{tor} and E^{pol}. Therefore, (A) and (B) do not hinder the quasiperiodic large-scale fluctuations.

IV. CONCLUSIONS

We have revealed the mechanism of the quasiperiodic behavior observed in von Kármán swirling flow driven by two smooth disks, which explains the origin of the nontrivial clockwise cycle observed in the P_{vis}-ϵ plot [Fig. 2(b)]. One of the most important findings is the significant quasiperiodic energy cycle (Table II) due to the energy exchange between the toroidal E^{tor} and poloidal E^{pol} components: (i) When E^{tor} is small, the toroidal velocity and toroidal-poloidal energy transfer $\mathcal{T}^{\text{tp}}$ are also small [Fig. 3(a)]. Then, because of the large shear rates on the rotating disks, the viscous stirring (i.e., P_{vis}) develops the toroidal flow. (ii) It triggers the centrifugal instability to generate $\mathcal{T}^{\text{tp}}$ with finite time delay [Fig. 3(a)]. (iii) Then, $\mathcal{T}^{\text{tp}}$ drives the increase of E^{pol} [Fig. 3(b)]. These processes generate the phase difference between E^{tor} and E^{pol} [Fig. 3(c)]. (iv) The development of the vortical structures (Fig. 9 in Appendix A) with the growing E^{pol} triggers the energy dissipation around them [Fig. 3(b)]. (v) At the same time, E^{tor} decreases as E^{pol} develops due to the angular momentum transfer. We have also demonstrated that the quasiperiodic cycle is observed in a range of Re ($1000 \leqslant$ Re $\leqslant 3000$; Fig. 7), which is well beyond the first Hopf bifurcation at Re ≈ 350 [24]. Although turbulence in the examined range of Re is not fully developed, we speculate that the proposed picture may hold for higher Re, as discussed in Sec. III D.

Here, we compare this energy cycle with that observed in turbulence [1,2] driven by steady force in a periodic box. In the present system, the cycle is sustained by the energy exchange between

the toroidal and poloidal components through centrifugal instability and the angular momentum transfer. On the other hand, the cycle in the periodic turbulence is sustained by the energy exchange between the largest-scale vortices and smaller ones through the energy cascade [3]. Therefore, the cause seems different. Nevertheless, since the nonnegligible temporal fluctuations of the energy transfer rate (i.e., $\mathcal{T}^{\mathrm{tp}}$ in the present system) lead to the temporal fluctuations of the interscale energy flux and dissipation rate, these cycles are equally important for the description of the nonequilibrium statistics of turbulence.

Besides, fluctuations of ϵ_{bou} (which determine the fluctuations of ϵ) exhibit the antiphase synchronization with $E_{\mathrm{bou}}^{\mathrm{tor}}$ (which has less impact on the fluctuations of E^{tor}, Fig. 5). Therefore, the nontrivial phase difference between P_{vis} and ϵ [Fig. 2(b)] is explained by these two findings: (i) there is a finite-time delay in the temporal evolution of P_{vis} and E^{tor}, and (ii) the phase of ϵ does not determine the phase of E^{tor}. Here, it is worth mentioning that this conclusion is related to the seminal experiments by Cadot *et al.* [5]; it is essential to distinguish the boundary and bulk regions to understand dynamics and statistics of the viscous-stirring von Kármán turbulence.

Before closing the present paper, we briefly discuss the case of inertial stirring. We expect that the mechanism in the inertial-driven case [14] is also described by the same process. The bladed disks generate much stronger E^{tor}, and thus the contribution of the viscosity is much smaller so that the boundary-bulk decomposition would not be necessary. Also, the generation mechanism of E^{tor} and the energy exchanges mechanism between E^{tor} and E^{pol} are independent of Re and the proposed picture may hold even for higher Re.

APPENDIX A: DYNAMICS OF THE POLOIDAL COMPONENTS

In this Appendix, we examine in more detail the dynamics of the poloidal components E^{pol} and ϵ^{pol} shown in Fig. 3(b). Figure 8(a) shows the time series of E^{pol} and its boundary-bulk decomposed components by (12). We see that $E^{\mathrm{pol}} \approx E_{\mathrm{bulk}}^{\mathrm{pol}}$; namely, E^{pol} is predominantly determined by its bulk component. Figure 8(b) shows that $E_{\mathrm{bulk}}^{\mathrm{pol}}$ and $\epsilon_{\mathrm{bulk}}^{\mathrm{pol}}$ are almost perfectly synchronized. This implies that, in the bulk of the system, the energy transferred to the poloidal component dissipates
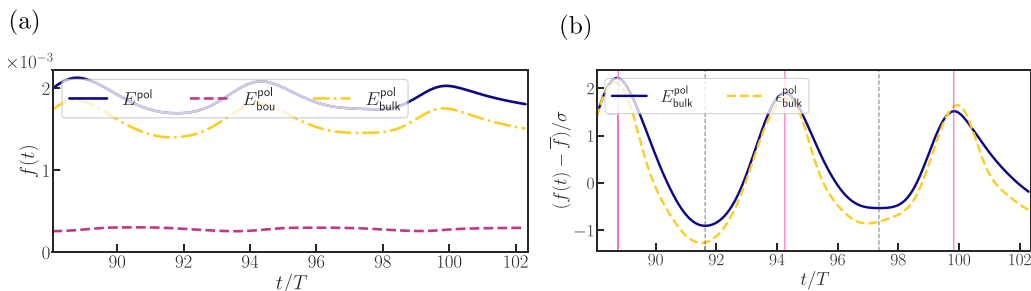
FIG. 8. Time series of (a) E^{pol}, $E_{\mathrm{bou}}^{\mathrm{pol}}$, $E_{\mathrm{bulk}}^{\mathrm{pol}}$, (b) $E_{\mathrm{bulk}}^{\mathrm{pol}}$, and $\epsilon_{\mathrm{bulk}}^{\mathrm{pol}}$. Pink and grey vertical lines indicate the local maxima and minima of $E_{\mathrm{bulk}}^{\mathrm{pol}}$. The time average and standard deviation of each quantity are shown in Table I. Results for Re = 1500.
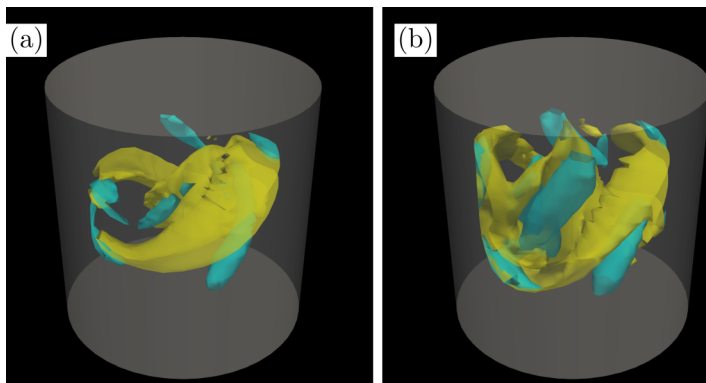
FIG. 9. Snapshots of isosurfaces of $Q = 0.3$ (light blue) and $S_{ij}S_{ij} = 0.4$ (yellow). Structures in the regions near the rotating disks ($|z| \geqslant 0.7R$) and side wall ($r \geqslant 0.75R$) are removed for visibility. (a) At $t/T = 91.6$ when $E_{\mathrm{bulk}}^{\mathrm{pol}}$ takes its local minimum; (b) $t/T = 94.3$ when it takes the local maximum. Results for Re $= 1500$.

immediately around the vortices (see Fig. 9, below) relevant to $E_{\mathrm{bulk}}^{\mathrm{pol}}$. In other words, the short time delay observed in Fig. 3(b) between E^{pol} and ϵ^{pol} does not imply an energy cascade event. Note that the synchronization between $E_{\mathrm{bulk}}^{\mathrm{pol}}$ and $\epsilon_{\mathrm{bulk}}^{\mathrm{pol}}$ is due to the smallness of the Reynolds number. For higher Reynolds numbers, smaller vortices are generated from the ones observed in Fig. 9, and $\epsilon_{\mathrm{bulk}}^{\mathrm{pol}}$ has a time delay to $E_{\mathrm{bulk}}^{\mathrm{pol}}$.

Figure 9 shows two snapshots of isosurfaces of the second invariant $Q = \Omega_{ij}\Omega_{ij} - S_{ij}S_{ij}$ of the velocity gradient tensor and $S_{ij}S_{ij}$ when $E_{\mathrm{bulk}}^{\mathrm{pol}}$ takes its local minimum and maximum. When $E_{\mathrm{bulk}}^{\mathrm{pol}}$ takes its local minimum, the flow has rather weak vortices and the strain-rate-dominant structures are disklike due to the toroidal flow [Fig. 9(a)]. On the other hand, the local maximum of $E_{\mathrm{bulk}}^{\mathrm{pol}}$ corresponds to the energetic vortices and the strain-rate-dominant structures fill their voids [Fig. 9(b)], which is relevant to the increase of $\epsilon_{\mathrm{bulk}}^{\mathrm{pol}}$.
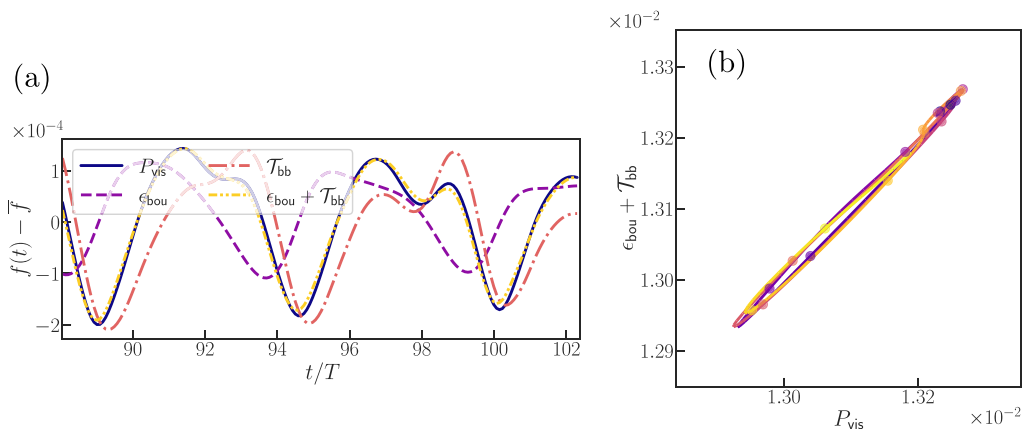
FIG. 10. (a) Time series of the quantities on the RHS of (B1) in the boundary region of the flow: the energy input rate P_{vis}, the energy dissipation rate ϵ_{bou}, the energy transfer rate from the boundary to the bulk regions $\mathcal{T}_{\mathrm{bb}}$, and $\epsilon_{\mathrm{bou}} + \mathcal{T}_{\mathrm{bb}}$. (b) 2D diagram of P_{vis} and $\epsilon_{\mathrm{bou}} + \mathcal{T}_{\mathrm{bb}}$. The time average and standard deviation of each quantity are shown in Table I. Results for Re $= 1500$.
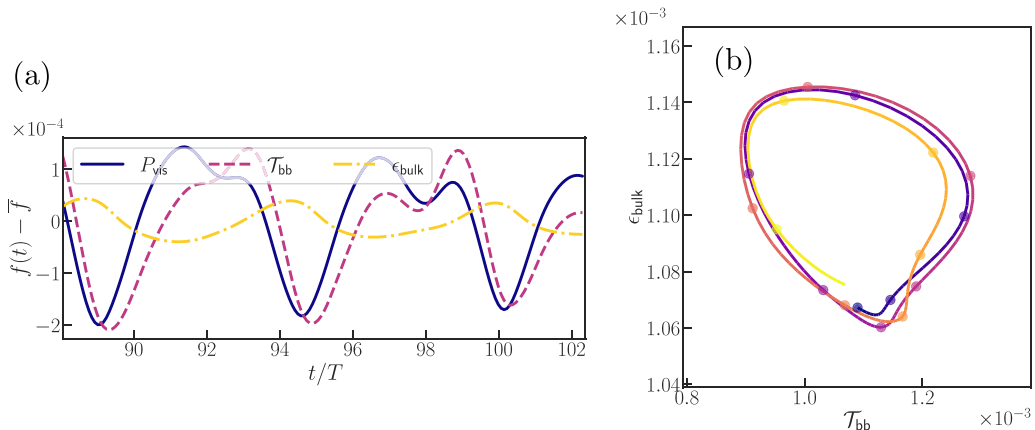
FIG. 11. (a) Time series of the quantities on the RHS of (B2) in the bulk region of the flow: the energy transfer $\mathcal{T}_{bb}$ from the boundary to the bulk regions and the energy dissipation rate ϵ_{bulk}. The energy input rate P_{vis} is also plotted for reference. (b) 2D diagram of $\mathcal{T}_{bb}$ and ϵ_{bulk}. The time average and standard deviation of each quantity are shown in Table I. Results for Re $= 1500$.

APPENDIX B: BOUNDARY-BULK DECOMPOSITION AND DYNAMICS OF EACH REGION

According to the boundary-bulk decomposition, we reformulate the energy equation in each region as

$$\frac{dE_{bou}}{dt} = P_{vis} - \epsilon_{bou} - \mathcal{T}_{bb}, \tag{B1}$$

$$\frac{dE_{bulk}}{dt} = \mathcal{T}_{bb} - \epsilon_{bulk}, \tag{B2}$$

where $\mathcal{T}_{bb}$ denotes the energy transfer from the boundary to the bulk regions.

First, we plot each term on the right-hand side (RHS) of (B1) in Fig. 10. We see well synchronized fluctuations of the energy input rate P_{vis} and the sum $\epsilon_{bou} + \mathcal{T}_{bb}$ of the energy dissipation rate and the energy transfer. This implies that the energy injected in the boundary region is instantaneously dissipated or transferred to the bulk region [Fig. 10(b)]. In this sense, the energy is balanced in the boundary region.

Next, we plot each term on the RHS of (B2) along with P_{vis} in Fig. 11. It is clear in Fig. 11(a) that these quantities attain their local maxima in order of P_{vis}, $\mathcal{T}_{bb}$, and ϵ_{bulk}. We also see an anticlockwise evolution in the $\mathcal{T}_{bb}$-ϵ_{bulk} diagram [Fig. 11(b)], implying the time-delayed correlation of these two quantities. This is consistent with the time-delayed dynamics, which we discuss in the main text in detail, in the bulk of the system.

[1] T. Yasuda, S. Goto, and G. Kawahara, Quasi-cyclic evolution of turbulence driven by a steady force in a periodic cube, Fluid Dyn. Res. **46**, 061413 (2014).

[2] S. Goto, Y. Saito, and G. Kawahara, Hierarchy of antiparallel vortex tubes in spatially periodic turbulence at high Reynolds numbers, Phys. Rev. Fluids **2**, 064603 (2017).

[3] S. Goto and J. C. Vassilicos, Local equilibrium hypothesis and Taylor's dissipation law, Fluid Dyn. Res. **48**, 021402 (2016).

[4] J. C. Vassilicos, Dissipation in turbulent flows, Annu. Rev. Fluid Mech. **47**, 95 (2015).

[5] O. Cadot, Y. Couder, A. Daerr, S. Douady, and A. Tsinober, Energy injection in closed turbulent flows: Stirring through boundary layers versus inertial stirring, Phys. Rev. E **56**, 427 (1997).

[6] N. Mordant, J. Delour, E. Léveque, A. Arnéodo, and J. F. Pinton, Long Time Correlations In Lagrangian Dynamics: A Key To Intermittency In Turbulence, Phys. Rev. Lett. **89**, 254502 (2002).

[7] E. W. Saw, D. Kuzzay, D. Faranda, A. Guittonneau, F. Daviaud, C. Wiertel-Gasquet, V. Padilla, and B. Dubrulle, Experimental characterization of extreme events of inertial dissipation in a turbulent swirling flow, Nat. Commun. **7**, 12466 (2016).

[8] P. Debue, V. Shukla, D. Kuzzay, D. Faranda, E. W. Saw, F. Daviaud, and B. Dubrulle, Dissipation, intermittency, and singularities in incompressible turbulent flows, Phys. Rev. E **97**, 053101 (2018).

[9] B. Dubrulle, Beyond Kolmogorov cascades, J. Fluid Mech. **867**, P1 (2019).

[10] A. N. Knutsen, P. Baj, J. M. Lawson, E. Bodenschatz, J. R. Dawson, and N. A. Worth, The inter-scale energy budget in a von Kármán mixing flow, J. Fluid Mech. **895**, A11 (2020).

[11] F. Ravelet, L. Marié, A. Chiffaudel, and F. Daviaud, Multistability And Memory Effect In A Highly Turbulent Flow: Experimental Evidence For A Global Bifurcation, Phys. Rev. Lett. **93**, 164501 (2004).

[12] A. De La Torre and J. Burguete, Slow Dynamics In A Turbulent Von Kármán Swirling Flow, Phys. Rev. Lett. **99**, 054101 (2007).

[13] R. Labbé, J. F. Pinton, and S. Fauve, Study of the von Kármán flow between coaxial corotating disks, Phys. Fluids **8**, 914 (1996).

[14] J. F. Pinton, P. C. W. Holdsworth, and R. Labbé, Power fluctuations in a closed turbulent shear flow, Phys. Rev. E **60**, R2452 (1999).

[15] J. H. Titon and O. Cadot, The statistics of power injected in a closed turbulent flow: Constant torque forcing versus constant velocity forcing, Phys. Fluids **15**, 625 (2003).

[16] S. Aumaître, S. Fauve, and J. F. Pinton, Large scale correlations for energy injection mechanisms in swirling turbulent flows, Eur. J. Mech. Fluids **16**, 563 (2000).

[17] L. Marié and F. Daviaud, Experimental measurement of the scale-by-scale momentum transport budget in a turbulent shear flow, Phys. Fluids **16**, 457 (2004).

[18] D. Kuzzay, D. Faranda, and B. Dubrulle, Global vs local energy dissipation: The energy cycle of the turbulent von Kármán flow, Phys. Fluids **27**, 075105 (2015).

[19] F. Ravelet, Bifurcations globales hydrodynamiques et magnétohydrodynamiques dans un écoulement de von Kármán turbulent, Ph.D. thesis, Ecole Polytechnique, 2005.

[20] C. Nore, D. Castanon Quiroz, L. Cappanera, and J. L. Guermond, Direct numerical simulation of the axial dipolar dynamo in the von Kármán Sodium experiment, Europhys. Lett. **114**, 65002 (2016).

[21] C. Nore, D. Castanon Quiroz, L. Cappanera, and J.-L. Guermond, Numerical simulation of the von Kármán sodium dynamo experiment, J. Fluid Mech. **854**, 164 (2018).

[22] S. Poncet, R. Schiestel, and R. Monchaux, Turbulence modeling of the Von Kármán flow: Viscous and inertial stirrings, Int. J. Heat Fluid Flow **29**, 62 (2008).

[23] S. Kreuzahler, D. Schulz, H. Homann, Y. Ponty, and R. Grauer, Numerical study of impeller-driven von Kármán flows via a volume penalization method, New J. Phys. **16**, 103001 (2014).

[24] C. Nore, M. Tartar, O. Daube, and L. S. Tuckerman, Survey of instability thresholds of flow between exactly counter-rotating disks, J. Fluid Mech. **511**, 45 (2004).

[25] W. Z. Shen, J. N. Sørensen, and J. A. Michelsen, Numerical study of swirling flow in a cylinder with rotating top and bottom, Phys. Fluids **18**, 64 (2006).

[26] A. Y. Gelfgat, P. Z. Bar-Yoseph, and A. Solan, Steady states and oscillatory instability of swirling flow in a cylinder with rotating top and bottom, Phys. Fluids **8**, 2614 (1996).

[27] P. Dimotakis, The mixing transition in turbulent flows, J. Fluid Mech. **409**, 69 (2000).

[28] H. M. Blackburn and S. J. Sherwin, Formulation of a Galerkin spectral element-Fourier method for three-dimensional incompressible flows in cylindrical geometries, J. Comput. Phys. **197**, 759 (2004).

[29] A. Bolis, C. D. Cantwell, D. C. Moxey, D. Serson, and S. J. Sherwin, An adaptable parallel algorithm for the direct numerical simulation of incompressible turbulent flows using a Fourier spectral/ hp element method and MPI virtual topologies, Comput. Phys. Commun. **206**, 17 (2016).

[30] G. Karniadakis and S. Sherwin, *Spectral/hp Element Methods for Computational Fluid Dynamics: Second Edition*, Numerical Mathematics and Scientific Computation (Oxford University Press, Oxford, 2005).